

Multiple Coiling of an Elastic Sheet in a Tube

Author(s): V. Romero, T. A. Witten and E. Cerda

Source: *Proceedings: Mathematical, Physical and Engineering Sciences*, Vol. 464, No. 2099 (Nov. 8, 2008), pp. 2847-2866

Published by: Royal Society

Stable URL: <https://www.jstor.org/stable/20209568>

Accessed: 31-01-2020 22:30 UTC

## REFERENCES

Linked references are available on JSTOR for this article:

[https://www.jstor.org/stable/20209568?seq=1&cid=pdf-reference#references\\_tab\\_contents](https://www.jstor.org/stable/20209568?seq=1&cid=pdf-reference#references_tab_contents)

You may need to log in to JSTOR to access the linked references.

---

JSTOR is a not-for-profit service that helps scholars, researchers, and students discover, use, and build upon a wide range of content in a trusted digital archive. We use information technology and tools to increase productivity and facilitate new forms of scholarship. For more information about JSTOR, please contact [support@jstor.org](mailto:support@jstor.org).

Your use of the JSTOR archive indicates your acceptance of the Terms & Conditions of Use, available at <https://about.jstor.org/terms>



JSTOR

*Royal Society* is collaborating with JSTOR to digitize, preserve and extend access to *Proceedings: Mathematical, Physical and Engineering Sciences*

## Multiple coiling of an elastic sheet in a tube

BY V. ROMERO<sup>1</sup>, T. A. WITTEN<sup>2</sup> AND E. CERDA<sup>1,\*</sup>

<sup>1</sup>*Departamento de Física, Universidad de Santiago de Chile, Avenida Ecuador 3493, Casilla 307, Correo 2, Santiago-Chile*

<sup>2</sup>*James Franck Institute and Department of Physics, University of Chicago, 929 East 57th Street, Chicago, IL 60637, USA*

A piece of paper coiled up in a tube hugs the wall in order to minimize its elastic energy. However, a moment's observation shows that the paper fails to make complete contact near its ends. Here, we show that the detached region in the inner part of the coil touches down the tube wall in an angle that is independent of the system size, thickness and stiffness of the surface. This angle is universal for any coiled sheet whose unstressed state is initially flat. Our results show how the shape and stress distribution for this detached region define the geometry and mechanical equilibrium for the rest of the sheet. In particular, we find scaling relations to describe the structure of the outer part of the coil, in contact with the tube wall, as a function of the number of times the sheet is coiled,  $N$ .

**Keywords:** folding; coiling; packing; crumpling; elasticity

### 1. Introduction

A huge 50 m steel strip produced in a factory must be packed into a roll of 1 m diameter before it is sent to the market. The genetic code of a virus encrypted in a DNA molecule of approximately  $10^2 \mu\text{m}$  length is carefully packed into a tiny capsule of 50 nm width. To coil a surface or fibre is one of the simplest ways of packing that does not require lines of high curvature or point singularities, where strains are important and plastic deformation or fracture can spoil the system (Witten & Li 1993; Cerda *et al.* 1999; Boué *et al.* 2006; Witten 2007). Although we normally pack surfaces by coiling, the description of the shapes observed is technically difficult. The main problem is self-contact. Even if the surface is assumed elastic and partial differential equations describe its local deformation, two points far from each other can make contact and produce a non-local interaction of the whole system. The simplest way to study the phenomena of coiling is to put the surface inside a tube of radius  $R$ , as we show in figure 1. The surface is coiled into a roll of smaller diameter than the tube, introduced into the tube and then released inside. It will hug the wall of the tube in order to minimize its elastic energy and conform to the geometry of the frame.

A crucial observation is made by looking at the innermost layer. It fails to make complete contact with the coil. The sheet detaches from a point, and then its end meets the envelope surface in a peculiar way (figure 1). The tangents to

\* Author for correspondence (ecerda@lauca.usach.cl).

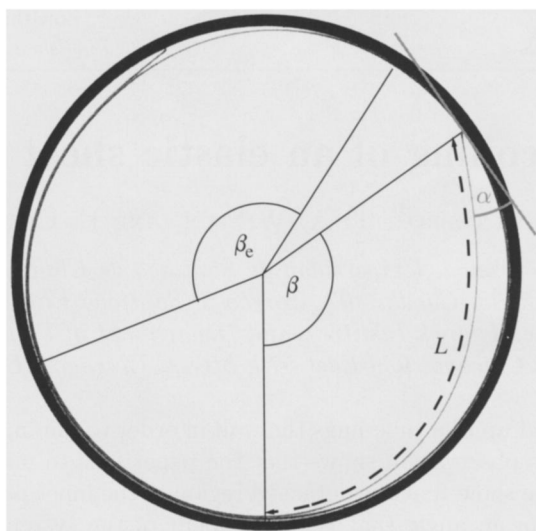


Figure 1. Photograph of a coiled sheet for  $R/S=0.188$ . The length of the sheet is more than 10 times the diameter and  $N=1$ .

the inner end of the sheet and the tangent to the tube intersect at this touchdown point, and define an angle  $\alpha$ . Later on, we will explain why this detachment is necessary for the equilibrium of the coil, but now we concentrate on its universality. Because the surface is bent and not stretched along its middle surface, the only material property that is necessary to describe the deformation is its bending stiffness,  $B$ . The thickness of the surface,  $t$ , plays a pure geometrical role: the coil becomes thicker in proportion to the length of the confined sheet,  $2S$ . Here, however, we focus on the case where thickness is negligible, so that most of the sheet follows the contour of the tube wall and is packed into a coil of curvature  $1/R$ . Thus, the mechanical properties of the detached region cannot depend on the total length of the sheet and its thickness. We conclude that a relation of the form  $\alpha=\alpha(B, R)$  is only dimensionally correct if this angle has a constant value or  $\alpha=\text{const}$ . This value must be the same for any elastic material and system size. A similar analysis implies that the opening angle subtended by the detached region,  $\beta$ , and the relative length of this segment to the radius of the tube,  $L/R$ , are also universal constants.

A similar phenomenon is observed in the outer part of the coil, where the outermost layer takes off at some point and touches down the wall. However, as the number of layers increases, more and more pressure is added to the tube, so that the angle subtended by the outer detached region,  $\beta_e$ , must decrease with the length of the sheet. If we define the number of times the sheet is coiled as  $N=[S/\pi R]$  (here  $[\cdot]$  denotes the integer part), dimensional analysis shows that  $\beta_e$  must be a function of  $N$ .

In the last years, two-dimensional packing of fibres and sheets has been studied for plastic (Donato *et al.* 2002, 2003) and elastic materials (Roman & Pocheau 1999; Boué *et al.* 2006; Boué & Katzav 2007). Crumpled plastic materials show a complex geometry consisting of folds or loops of different curvature in a distribution that needs a proper statistical analysis. The final shape of the fibre or sheet will greatly depend on the way the system is prepared. On the other

hand, a confined elastic fibre or sheet will search for a configuration that minimizes its elastic energy. This self-organization leads to simple structures, such as the ‘ying-yang’-like shape reported by Boué *et al.* (2006) when packing a sheet inside a rigid cylinder. As the same authors concluded, this shape is observed because a closed fibre is constrained inside a cylinder; however, a spiral of pitch  $t$  must be the optimal packing for a fibre with two extremities. Figure 1 shows that this spiral shape, although simple, has some interesting features, such as the mentioned detached regions near the sheet ends. In the present paper, we show that these regions are necessary to obtain the torques that bend the sheet into a coil. In §2, we start with the analysis of a sheet with a sufficient number of layers such that the outer detached region is small ( $\beta_e \approx 0$ ). The deformation of the surface is studied in terms of the classical *Elastica* or Euler equation (Landau & Lifchitz 1997) with no friction between the layers or between the coil and the wall. Our analysis of this equation gives the universal angle  $\alpha$  and the length  $L$  of the detached region. In the same section, we prove that the system of forces acting in the innermost layer completely determines the stress in the whole sheet. This leads to the determination of the average pressure over the tube wall, the contact forces between different layers and the cross-sectional force in each layer. In §3, we study the Euler equation for early stages of confinement when the two ends of the sheet do not interact. Our solution shows how a symmetrical shape rests on two contact points with the tube wall, until a third contact point is necessary for equilibrium. Cohen & Mahadevan (2003) reported similar shapes for nanotubes inside water drops, although they stopped the analysis at this stage. When the radius is further decreased, the curvature at this new contact point matches the curvature of the tube and then a region of contact is developed. This region separates two detached regions that take on the universal properties described in §2. Continuing reduction of the radius simply expands this contact region. In §4, we study the case when both detached regions interact and then the universal shape is disrupted. One end of the sheet overlaps the other and presses the (now named) outer end against the wall. This end moves along the sheet until a new point of self-contact is observed. This point evolves into a region of contact when the curvatures of each side equalize. Again, this contacting region expands until one of its boundaries reaches the curvature of the tube wall. At this critical radius, the universal shape of the inner detached region is restored. In §5, we study how this mechanism is replicated to describe the deformation for any number of layers, so that the function  $\beta_e(N)$  is obtained. Finally, we close with a discussion of our results.

## 2. The geometry of the innermost layer

### (a) *Equilibrium equations and geometry*

For planar deformations one of the principal curvatures of the sheet vanishes, so that its line of curvature is a straight line or generator. The other line of curvature lies in a plane, so that this line defines a two-dimensional curve. In Cartesian coordinates, the position vector describing the geometry of the curve can be written as  $\mathbf{r}(s) = x(s)\mathbf{e}_1 + y(s)\mathbf{e}_2$ , as we show in figure 2. Here,  $s$  is the arc length of the curve starting from the take-off point, and  $\mathbf{e}_1$  and  $\mathbf{e}_2$  are two perpendicular unit vectors lying in the plane. The tangent to the curve is readily

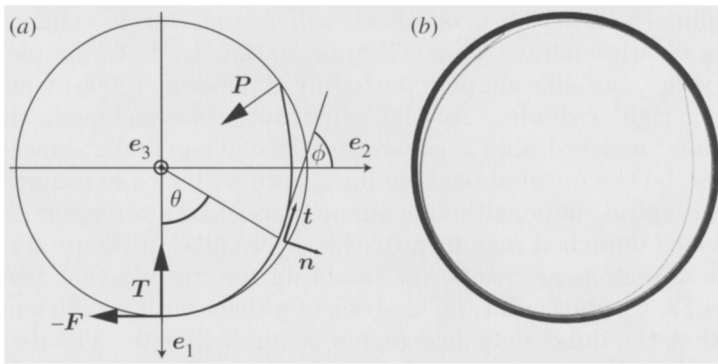


Figure 2. (a) Geometry of a sheet coiled in a cylindrical tube. The deformation can be described by using a two-dimensional system of coordinates with its origin at the centre of the tube. The angle  $\phi$  gives the position of the tangent with respect to the horizontal direction. The trihedrons  $\{e_1, e_2, e_3\}$  and  $\{n, t, e_3\}$  are defined in the figure. (b) A coil made of mica with similar geometry as (a).

obtained as  $t = \partial_s r$ , and its normal as  $n = t \times e_3$ , where  $e_3 = e_1 \times e_2$  points along the generator. The curvature of the principal line is then  $\kappa = -n \cdot \partial_s t$  (Struik 1988). Now, we proceed to write the equations of force and torque equilibrium (Love 1944; Landau & Lifshitz 1997; Cerda & Mahadevan 2005),

$$\text{and } \left. \begin{aligned} \partial_s F + K &= 0 \\ \partial_s M + t \times F &= 0, \end{aligned} \right\} \tag{2.1}$$

where  $K$  is the external force per unit of area applied over the surface;  $F$  is the force resultant on a cross section; and  $M$  is the torque resultant per unit of length. A constitutive relation is needed to solve the equations. The torques can be connected with the curvature by the Bernoulli–Euler theorem; torques are proportional to the local curvature. The precise relation for planar deformations is  $M = B\kappa e_3$  (Love 1944; Landau & Lifshitz 1997). We introduce the angle  $\phi$  that the tangent to the curve makes with the vector  $e_2$ . In terms of this angle, the tangent and the normal are  $t = -\sin \phi e_1 + \cos \phi e_2$  and  $n = \cos \phi e_1 + \sin \phi e_2$ . This allows us to find the curvature as  $\kappa = -n \cdot \partial_s t = \dot{\phi}$ .

We now turn to the determination of the shape of the innermost layer. The  $e_1$  axis was made to cross the sheet at the position of the take-off point in figure 2. In this configuration, it is straightforward to obtain the force balance in equilibrium.

We first note that the force  $F$  that the rest of the sheet at the left side of the take-off point applies to the detached segment must be horizontal. To the left side of the take-off point, the sheet follows the circular shape of the container and thus has constant curvature. Therefore, in this region  $\partial_s M = 0$  and the torque balance equation (2.1) yields  $t \times F = 0$ . Thus, the force at the cross section has the direction of the tangent and can be written as  $F = -ft$  for  $s < 0$ , or  $F = -fe_2$  when approaching the take-off point from the left side, where the negative sign is due to the orientation chosen for the cross section that points in the same direction as the tangent  $t$ . Furthermore, the external force per unit width at touchdown,  $P$ , points to the centre of the tube since it is exerted by the frictionless wall. Then,  $P = -P(\cos \beta e_1 + \sin \beta e_2)$ . Here we observe that the horizontal component of the force at the touchdown point is balanced by force  $F$ , but not

its vertical component. Hence, a vertical point force is needed for equilibrium at the take-off point. This force,  $\mathbf{T}$ , is also provided by the wall, so that it must have the normal direction to the wall at this point. It gives  $\mathbf{T} = -T\mathbf{e}_1$ . Thus, force balance dictates the following relations between forces:

$$T = -P \cos \beta \quad \text{and} \quad f = P \sin \beta. \quad (2.2)$$

Both relations show that balance is possible only if the angle  $\beta$  is in the second quadrant, i.e. between  $\pi/2$  and  $\pi$ . To obtain the angle  $\beta$ , we need to solve the equations of equilibrium for the sheet. The segment is free of external forces between the take-off point and the touchdown point, so that the cross-sectional force  $\mathbf{F}$  must be a constant along the segment. Its value is obtained by direct integration of the first of the equations in (2.1) near the touchdown point. It yields  $\mathbf{F} = \mathbf{P}$  for  $0 < s < L$ . The second equation for torque balance gives the Euler equation,

$$B\ddot{\phi} + P \cos(\phi - \beta) = 0. \quad (2.3)$$

This is the same equation for a pendulum with frequency  $\omega^2 = P/B$ , hence it is solved in terms of elliptic functions. A first integration yields  $B\dot{\phi}^2/2 - P[\sin(\beta - \phi) - \sin \alpha] = 0$ . This represents the sum of kinetic and potential energy for the case of a pendulum. Here, we have used the conditions that no torques are applied at the touchdown point, where the tangent is  $\phi = \beta - \alpha$ , so that the sheet near this point has zero curvature and must be straight. There is another constraint. The torque resultant at the take-off point must be continuous across the contact point, so that  $\dot{\phi}|_{\phi=0} = 1/R$  (Mahadevan & Keller 1999; Cerda & Mahadevan 2005). We conclude that the force at the touchdown point can be written in terms of parameters related to the geometry of the detached segment  $PR^2/B = 1/[2(\sin \beta - \sin \alpha)]$ . Moreover, the curvature as a function of the angle is now given by  $R\dot{\phi} = [\sin(\beta - \phi) - \sin \alpha]^{1/2}/[\sin \beta - \sin \alpha]^{1/2}$ .

A final requirement is that the touchdown and take-off point are located in the positions  $(x, y) = R(\cos \beta, \sin \beta)$  and  $(x, y) = R(1, 0)$ , respectively. This gives two conditions that allow the determination of the angles  $\alpha$  and  $\beta$ . The kinematic relation  $\mathbf{t} = \partial_s \mathbf{r}$  yields  $\dot{x} = -\sin \phi$ ,  $\dot{y} = \cos \phi$ ; hence, after a change of variables from the arc length to the tangent angle, we obtain the shape of the segment as

$$x = -\int_0^\phi d\phi \frac{\sin \phi}{\dot{\phi}} + R \quad \text{and} \quad y = \int_0^\phi d\phi \frac{\cos \phi}{\dot{\phi}}. \quad (2.4)$$

The evaluation of these relations at the angle  $\phi = \beta - \alpha$  gives the required conditions. Combining both relations, we find that the opening angle and the take-off angle are related through the equation  $2 \sin \alpha = \sin \beta$ . This defines the multivalued function  $\beta = \beta(\alpha)$ . A second equation gives the value of  $\alpha$  after solving the transcendental relation

$$\int_\alpha^{\beta(\alpha)} dz \frac{\sin z}{\sqrt{\sin z - \sin \alpha}} = \frac{1 - \cos(\beta(\alpha))}{\sqrt{\sin \alpha}}. \quad (2.5)$$

A numerical evaluation of this relation yields the value of the take-off angle as  $\alpha \approx 0.421$  ( $\approx 24.1^\circ$ ) and the opening angle as  $\beta \approx 2.185$  ( $\approx 125.2^\circ$ ). Using the identity  $2 \sin \alpha = \sin \beta$ , we obtain the touchdown force as  $PR^2/B = 1/\sin \beta \approx 1.224$ . Equation (2.2) gives, for the cross-sectional pressure, the simple expression

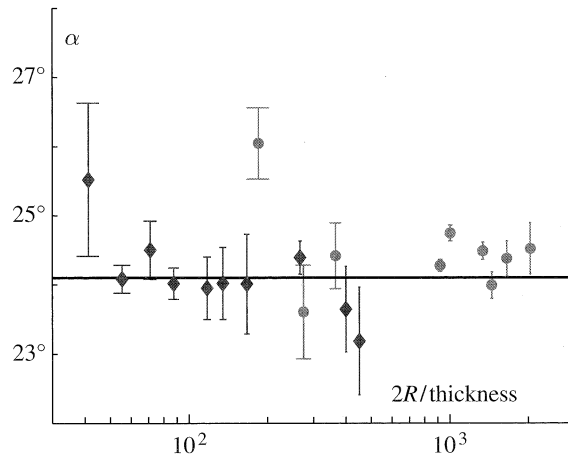


Figure 3. Measured touchdown angle for different materials and confining radii  $R$ , illustrating universality of  $\alpha$ . Circles, amorphous metal ribbon of 0.002 cm thickness and 0.5 cm width; diamonds, mica strip of 0.02 cm thickness and 1 cm width. Upper error bound indicates the angle at the contact point and lower error bound is the angle extrapolated from the inner surface of the strip to the boundary. Thick horizontal line indicates the predicted universal value of  $\alpha$ .

$fR^2/B = 1$  and, for the take-off force,  $TR^2/B = -1/\tan \beta \approx 0.705$ . Moreover, the length of the segment is  $L = \int_0^{\beta-\alpha} d\phi 1/\dot{\phi}$ , i.e.  $L/R = 2.089$ . The segment is a little longer than the diameter of the tube.

To check experimentally the value of the angle  $\alpha$ , we have coiled a strip of mica and an amorphous metal ribbon inside tubes of variable radius. Since friction opposes the relaxation of the sheet to the equilibrium state predicted in our analysis, the tube was vibrated to allow the edge to find its minimum-energy position. Photographs were taken with the camera centred on the take-off point, so that the measured angle is not affected by perspective effects.<sup>1</sup> The mica and metal have thickness of  $t = 0.2$  mm and 20  $\mu\text{m}$ , respectively. Since the sheet is straight near the touchdown point, it is not difficult to define its tangent line and obtain the intersection with the tangent line to the tube. A difficulty is that the tangent line can be plotted at any position across the thickness of the sheet and the choice can change the angle by two or three degrees. Two parallel lines make different angles with the tangent to the tube since they intersect the circle at different positions. Our choice was to measure two angles, one by using the line along the inner surface of the sheet, and the other by using the outer surface. The line closer to the centre gives the larger angle. Using these two values, we defined the angle  $\alpha$  as the mean value of the two and the error of our measurements by their difference.

The strip was coiled into tubes of decreasing radius until it failed to return to the straight state upon removal from the tube. Figure 3 shows our experimental results for both materials. The angle is near the theoretical value predicted over a wide range of values of the ratio  $2R/t$ , although a departure from the theory is observed for small diameters. We account for that change as a sign of plastic

<sup>1</sup> The angle can change by several degrees if the camera is centred on the centre of the tube owing to parallax error.

behaviour in the system. The bending strain is  $\gamma \approx t/R$ , so that the abscissa in figure 3 represents the inverse of this strain. The plastic limit was independently estimated by measuring the maximum value of the curvature such that the strip could not return to its initial state. For mica, we found the critical value  $\gamma_c = 0.025$ , which is consistent with the value  $2R/t \approx 100$ , where the departure from the theoretical angle was found for that material. We note that there is no plastic deformation in the detached segment except near the take-off point, so that the resisting torque at that region is lower than for the elastic case. Hence, the segment is less compressed against the wall and the touchdown angle must be larger than the one predicted (figure 3).

(b) *Forces in the coiled surface*

At the region of contact near the take-off point, the curvature of the sheet has the curvature of the tube  $1/R$ . Obviously, this is an approximation that assumes the sheet has zero thickness. Curvature should be slightly larger in proportion to the number of layers and thickness of the sheet. We also assume that there are sufficient numbers of loops to keep the outermost layer in close contact with the tube, so that  $\beta_e = 0$ . Since  $\partial_s \mathbf{M} = \mathbf{0}$ , the torque balance equation yields  $\mathbf{t} \times \mathbf{F} = \mathbf{0}$ , hence the force at the cross section has the direction of the tangent and can be written as  $\mathbf{F} = -f\mathbf{t}$ . Besides, the external force applied by the wall or the other layers must point along the normal, so that  $\mathbf{K} = -k\mathbf{n}$ . This external force is connected with the cross-sectional force by the first of the equations in (2.1). This connection is possible only if  $f$  and  $k$  are constants that satisfy the equation

$$k = \frac{f}{R}. \quad (2.6)$$

The value of  $f$  is fixed by continuity. Its value is  $fR^2/B = 1$  at the take-off point and must have the same value at every point of the coil. The net external force per unit of length over a given layer is then  $k = f/R = B/R^3$ . This is the sum of the normal forces applied by the inner and outer layers (or wall) in contact with it. Summing up all these contributions, we obtain that a coil of  $N$  layers pushes the wall with a pressure  $p$  given by

$$p = N \frac{B}{R^3}. \quad (2.7)$$

This result can be obtained in a more general framework by using the mean pressure defined in the work of Boué *et al.* (2006). The bending energy per unit of width of a small segment  $\Delta s$  of the sheet in close contact with the frame is proportional to  $(B/2)\Delta s/R^2$ . Neglecting the structure of the inner and outer layer, we conclude that the total elastic energy per unit of line must be  $U_B = (B/2)2S/R^2$  (Landau & Lifshitz 1997). The total area of the container is  $A = \pi R^2$ , hence the energy can be written in terms of this area as  $U_B = \pi BS/A$ . The average mechanical pressure over the wall is obtained from  $\bar{p} = -(\partial U_B / \partial A)_s$ . It again yields the result (2.7) after we replace  $N$  by  $S/\pi R$ . We will discuss more about the validity of connecting formula (2.7) with the average pressure in §5.

Our assumption that the curvature is constant and equal to  $1/R$  is not true when the outer end of the sheet separates from the coil and lifts all the other layers. In this case, we can show that our result (2.7) stands valid for the regions

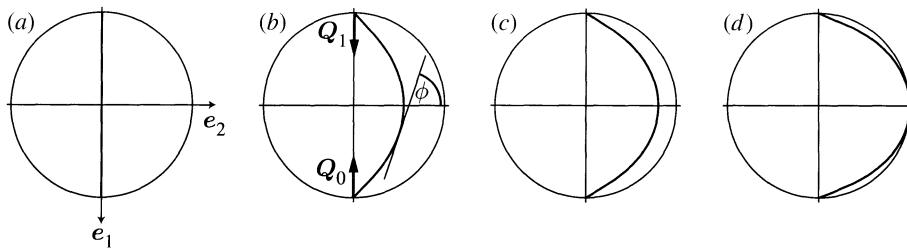


Figure 4. Schematic end views of a sheet of arc length  $2S$ . (a) The sheet touches the circle at the two ends when  $R/S=1$ . (b) Here, the radius is  $R/S=0.932$  and  $\phi_0=\pi/3$ . (c)  $R/S=0.741$  and  $\phi_0=\pi/6$ . (d) The midpoint first contacts the circle when  $R/S=\epsilon_1$ , where  $\epsilon_1$  is defined in the text. This new contact point is at the angle  $\phi=\pi/2$ .

in contact with the tube. To see that, we study the equations of equilibrium in intrinsic coordinates  $\mathbf{F}=f_t\mathbf{t}+f_n\mathbf{n}$ . The torque balance gives  $f_n=B\dot{\phi}$  and the force balance in the tangential direction is  $\dot{f}_t+\dot{\phi}f_n=0$ , since there are no frictional contact forces. Combining both equations, we obtain the relation  $\dot{f}_t+B\dot{\phi}\dot{\phi}=0$ . An integration yields

$$f_t = -\frac{B}{2}(\dot{\phi}^2 - \dot{\phi}_1^2) + f_1, \quad (2.8)$$

where  $\dot{\phi}_1$  and  $f_1$  are integration constants. Assuming that the innermost layer does not interact with the outer detached region because they are in different angular sectors (figure 2), we fix the constants by using the curvature and force at the take-off point. We obtain  $\dot{\phi}_1=1/R$  and  $f_1=f$ . Therefore, any layer with the same curvature will have the same cross-sectional force. In particular, if all the layers in a given section of the coil have approximately the curvature of the tube wall, we conclude that  $f_t=f$  and formula (2.7) remains valid at those locations.

### 3. Early stages of coiling

We now study the series of events that lead to the coiling of the sheet inside the tube as the radius  $R$  decreases from a large value. The minimal length needed for the sheet to exert force on the tube is the diameter  $2R$ . At this condition, we put the sheet along the direction  $\mathbf{e}_1$  for the axes defined in figure 4a. If the tube diameter is a bit smaller than the sheet length, the sheet starts to bend to one of the two sides of the tube as we observe in figure 4b. Note that both contact points must remain on the diameter line because this is the only way the external point forces  $\mathbf{Q}_0$  and  $\mathbf{Q}_1$  can add to zero.

The force  $\mathbf{Q}_0$  is normal to the contact point at the lower part of the strip and can be written as  $\mathbf{Q}_0=-q_0\mathbf{e}_1$ , where  $q_0$  is the magnitude of the force. It is straightforward to see that the equation for the curvature is  $B\ddot{\phi}-q_0\cos\phi=0$ . A first integration of this relation gives, for the curvature,

$$\dot{\phi} = (2q_0/B)^{1/2}(\sin\phi - \sin\phi_0)^{1/2}, \quad (3.1)$$

where  $\phi_0$  is the touchdown angle at the lower point. This angle is not the universal angle  $\alpha$  of §2. It decreases as the radius is reduced. Owing to the symmetry, we solve the equation between the angles  $\phi_0<\phi<\pi/2$ , where  $\phi=\pi/2$

is the point of maximum curvature along the sheet. That point moves along the line  $x=0$ , so that the total projected length along the vertical axis from the touchdown point to the point of maximum curvature is  $R$ . Evidently, the length of the strip between these two points is  $S$ . These two constraints give the value of the unknown parameters  $q_0$  and  $\phi_0$ . We obtain

$$R = \int_{\phi_0}^{\pi/2} d\phi \frac{\sin \phi}{\dot{\phi}} \quad \text{and} \quad S = \int_{\phi_0}^{\pi/2} d\phi \frac{1}{\dot{\phi}}. \quad (3.2)$$

Substituting the value of the curvature from equation (3.1), we eliminate the parameter  $q_0$  in favour of the angle  $\phi_0$ . It yields

$$R/S = \int_{\phi_0}^{\pi/2} d\phi \frac{\sin \phi}{\sqrt{\sin \phi - \sin \phi_0}} \bigg/ \int_{\phi_0}^{\pi/2} d\phi \frac{1}{\sqrt{\sin \phi - \sin \phi_0}}, \quad (3.3)$$

which defines the function  $\phi_0 = \phi_0(R/S)$ . This function can be replaced in the first equation in (3.2) to obtain the parameter  $q_0$ . It gives

$$R^2 q_0/B = \frac{1}{2} \left( \int_{\phi_0(R/S)}^{\pi/2} d\phi \frac{\sin \phi}{\sqrt{\sin \phi - \sin(\phi_0(R/S))}} \right)^2. \quad (3.4)$$

We note that the force  $R^2 q_0/B$  decreases as the radius is further decreased (figure 7*b*), so that the sheet is more easily bent by the tube. The average pressure is the sum of the magnitude of the normal forces divided by the perimeter. In this case, we obtain  $\bar{p} = 2q_0/(2\pi R)$ . This definition is equivalent to the expression  $\bar{p} = (\partial_A U_B)_S$  used in §2*b*. We note that the force  $R^2 q_0/B$  and the average pressure decrease as the radius is further decreased (figures 7*b* and 12), so that the sheet is more easily bent by the tube. In addition, the curvature of the midpoint decreases when  $R/S$  is reduced until the condition  $R/S = \epsilon_1 = 0.659$ . Here, the point at  $\phi = \pi/2$  makes contact with the frame (figure 4*d*). The angle  $\phi_0$  decreases from the value  $\phi_0 = \pi/2$ , where the sheet is straight, to the value  $\phi_0 \approx 0.358$  ( $\approx 20.5^\circ$ ).

We can see from figure 4*d* that our solution remains valid until the sheet touches the tube in the position  $(x, y) = (0, R)$ . At  $R/S = \epsilon_1$ , there are three external point forces over the surface such that  $\mathbf{Q}_0 + \mathbf{Q}_1 + \mathbf{Q}_2 = \mathbf{0}$  (figure 5*b*). Here, we name the point forces, tangent angles, arc length positions and points where they are located in anticlockwise order. The first point 0 is located at  $s=0$ , the tangent angle at this point is  $\phi_0$  and the point force is  $\mathbf{Q}_0$ ; the second point 1 is located at  $s=s_1$ , its tangent is  $\phi_1$  and the point force is  $\mathbf{Q}_1$ , etc., as we move along the sheet from the starting point at  $s=0$ . Owing to the rotational invariance of the system, we can fix point 0 in the vertical axis. Further decreases of the radius move point 2 out of the diametral line since the horizontal components of force  $\mathbf{Q}_1$  and  $\mathbf{Q}_2$  must cancel. The curvature is again given by  $B\dot{\phi}^2/2 = q_0(\sin \phi - \sin \phi_0)$ , but we need to apply different boundary conditions. The contact point at  $s=S$  is located at  $(x, y) = R(\cos \phi_1, \sin \phi_1)$ . That requirement gives the necessary conditions to find the parameters  $\{\phi_0, \phi_1\}$ . An integration of equation (2.4) applied to this

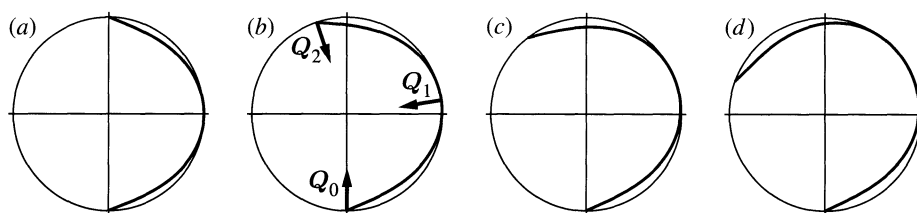


Figure 5. Sketch of the strip for  $\epsilon_2 < R/S < \epsilon_1$ . There are three point forces applied on the sheet at  $s=0$ ,  $S$  and  $2S$ . (a)  $R/S=\epsilon_1$  and (b)  $R/S=0.6$ . The upper end of the sheet moves to the left side of the line  $y=0$  to balance the horizontal force at the midpoint. (c)  $R/S=0.55$  and (d)  $R/S=\epsilon_2$ , where the curvature at the midpoint matches the curvature of the tube.

geometry gives, for the coordinates,

$$x/R = -\frac{1}{(2R^2 q_0/B)^{1/2}} \int_{\phi_0}^{\phi} d\phi \frac{\sin \phi}{\sqrt{\sin \phi - \sin \phi_0}} + 1$$

and

$$y/R = \frac{1}{(2R^2 q_0/B)^{1/2}} 2\sqrt{\sin \phi - \sin \phi_0}.$$

We evaluate the second relation at the new contact point to obtain the force  $q_0$  as a function of the unknown angles  $\phi_0$  and  $\phi_1$ . It gives  $R^2 q_0/B = 2(\sin \phi_1 - \sin \phi_0)/\sin^2 \phi_1$ . These two angles are found by using the conditions that the  $x$  position and length of the sheet at the angle  $\phi = \phi_1$  follow the relations

$$1 - \cos \phi_1 = \frac{\sin \phi_1}{2\sqrt{\sin \phi_1 - \sin \phi_0}} \int_{\phi_0}^{\phi_1} d\phi \frac{\sin \phi}{\sqrt{\sin \phi - \sin \phi_0}}$$

and

$$S/R = \frac{\sin \phi_1}{2\sqrt{\sin \phi_1 - \sin \phi_0}} \int_{\phi_0}^{\phi_1} d\phi \frac{1}{\sqrt{\sin \phi - \sin \phi_0}}.$$

Figure 5 shows the numerical solution of these equations for some values of the parameter  $R/S$ . In contrast with the first case, the curvature at the midpoint decreases and the angle  $\phi_0$  increases as the radius is further decreased.

Our solution is valid while the curvature of the midpoint is larger than the curvature of the tube. When they become equal, a region of contact is developed between the sheet and the wall. This region separates two similar detached regions that obey exactly the same boundary conditions that we used to obtain the universal shape in §2. Therefore, the sheet geometry is represented by two segments with universal shape connected by an angular region  $\phi$  (figure 6*b*) in contact with the tube. We readily obtain the values  $\phi_0 = \alpha$ ,  $\phi_1 = \beta$  and  $q_0 = P$  that we found in §2. There are a pair of point forces in each detached region and a distribution of forces at the contact region, as figure 6*b* shows. As the radius of the sheet decreases, the detached segments keep their shape and the region of contact expands. This solution is valid until point 3 meets point 0 in  $(x, y) = (R, 0)$ , as is shown in figure 6*d*. Since the detached segment spans an angle  $\beta$ , we conclude that the solution remains valid until the angular sector  $\phi$  equals the angle  $(2\pi - 2\beta)$ . It yields a value  $R/S = \epsilon_3 = 0.328$ . Finally, figure 7 summarizes the behaviour of the quantities  $\{\phi_0, \phi_1, q_0, q_1\}$  for the events described in this section.

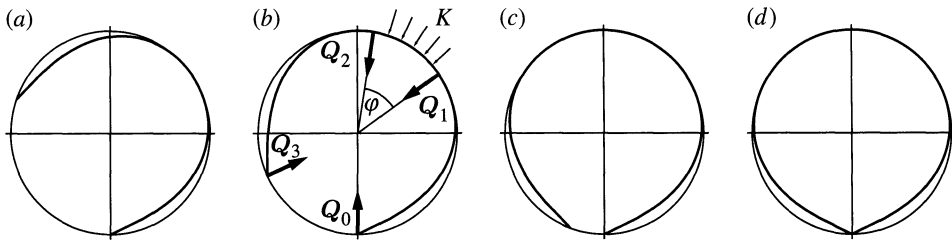


Figure 6. Sketch of the sheet for  $\epsilon_3 < R/S < \epsilon_2$ . (a)  $R/S = \epsilon_2$ , where the curvature at the midpoint is  $1/R$ . The detached region has a shape as shown in figure 2. (b) The contact point at  $s = S$  transforms into a region of contact that spans an angle  $\phi$ . Here,  $\phi = \pi/4$ , (c)  $\phi = \pi/4$  and (d)  $\phi = \pi/2$ . The two ends of the strip make contact at the line  $y = 0$ . The total angle of contact with the tube is  $\phi = 1.9$  ( $\approx 109^\circ$ ) and  $R/S = \epsilon_3$ .

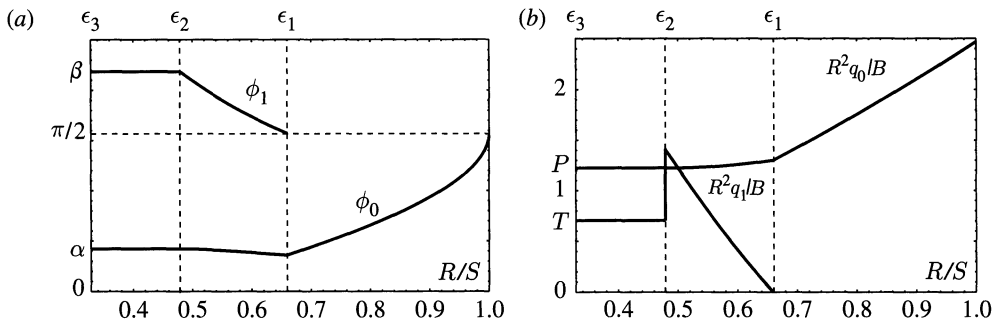


Figure 7. (a) The touchdown and take-off angles as the radius of the tube is reduced from  $R/S = 1$  to  $R/S = \epsilon_3$ . (b) The dimensionless touchdown and take-off point forces.

### 4. Self-contact

For  $S/R < \epsilon_3$ , the endpoint at  $s = 2S$  touches the end at  $s = 0$ . There are five point forces along the sheet, as figure 8b shows. These forces point perpendicular to the surface of contact, i.e.

$$\mathbf{Q}_0 = -q_0 \mathbf{e}_1, \quad \mathbf{Q}_1 = q_1 \mathbf{n}(\phi_1), \quad \mathbf{Q}_2 = -q_2 \mathbf{n}(\phi_2), \quad \mathbf{Q}_3 = -q_3 \mathbf{n}(\phi_3) \quad \text{and} \quad \mathbf{Q}_4 = -\mathbf{Q}_1.$$

Force balance requires that the total cross-sectional forces at points 2 and 3 must be tangential just above  $s_2$  ( $\mathbf{F}_2$ ) and just below  $s_3$  ( $\mathbf{F}_3$ ). Using the first of the equations in (2.1), we find the constraints

$$\mathbf{F}_2 = -f_2 \mathbf{t}(\phi_2) = -\mathbf{Q}_0 - \mathbf{Q}_1 - \mathbf{Q}_2$$

and

$$\mathbf{F}_3 = -f_3 \mathbf{t}(\phi_3) = \mathbf{Q}_3 + \mathbf{Q}_4.$$

The last two vectorial equations allow us to find the parameters  $\{q_0, q_1, q_2, q_3\}$  in terms of two parameters  $\{f_2, f_3\}$ . We now obtain the equations for each segment of the sheet. The cross-sectional force for  $0 < s < s_1$  is  $\mathbf{F} = -\mathbf{Q}_0$  and the tangent angle follows the equation  $B\ddot{\phi} - q_0 \cos \phi = 0$ . The next segment at  $s_1 < s < s_2$  has a cross-sectional force  $\mathbf{F} = -\mathbf{Q}_0 - \mathbf{Q}_1$  and its deflexion is given by the equation  $B\ddot{\phi} - q_0 \cos \phi + q_1 \cos(\phi - \phi_1) = 0$ . Finally, the cross-sectional force for  $s_3 < s < 2S$  is  $\mathbf{F} = -\mathbf{Q}_1$ , and this segment follows the equation  $B\ddot{\phi} + q_1 \cos(\phi - \phi_1) = 0$ .

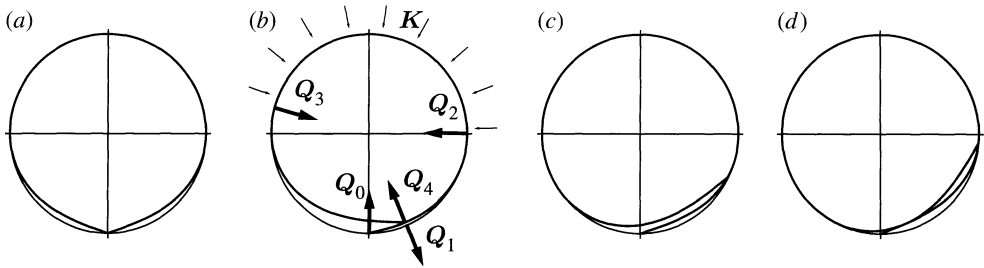


Figure 8. Sketch of the sheet for  $\epsilon_5 < R/S < \epsilon_4$ . (a)  $R/S = \epsilon_4$ , (b)  $R/S = 0.316$ , (c)  $R/S = 0.276$  and (d)  $R/S = \epsilon_5$ .

The shape of each segment is found by solving the equations for the curvature and the coordinates. If we define  $\kappa = \dot{\phi}$ , the equation for the curvature can be written as  $\dot{\kappa} = W(\phi)$ , where  $W(\phi)$  is a different function for each segment. Hence, an ordinary differential equation (ODE) system of four equations,

$$\dot{x} = -\sin \phi, \quad \dot{y} = \cos \phi, \quad \dot{\phi} = \kappa \quad \text{and} \quad \dot{\kappa} = W(\phi), \tag{4.1}$$

gives the shape of the segment. The flow defined by this ODE connects the coordinates  $\{x, y, \phi, \kappa\}$  at both ends for each segment, so that four constraints are obtained by solving the system. Since there are three different segments, a total of 12 conditions are obtained. On the other hand, we can completely define the coordinates of the endpoint of each segment by using the parameters  $\{\phi_0, \phi_1, \phi_2, \phi_3, \phi_4, x_1, y_1, \kappa_1\}$ . For instance, the coordinates of point 4 along the segment  $s_3 < s < 2S$  are  $\{x_1, y_1, \phi_4, 0\}$  and the coordinates of point 1 are  $\{x_1, y_1, \phi_1, \kappa_1\}$ . This set of unknowns must be added to the set of parameters  $\{f_2, f_3, s_1, s_2\}$  that are needed to solve the equations. Here, we do not include the arc length at point 3 since the sheet follows the wall between points 2 and 3 and then  $s_3 = s_2 + R(\phi_3 = \phi_2)$ . Thus, for a given value of the radius  $R$  and length  $2S$ , our unknowns are  $\{\phi_0, \phi_1, \phi_2, \phi_3, \phi_4, x_1, y_1, \kappa_1, f_2, f_3, s_1, s_2\}$ , a total of 12, and the problem is well posed.

A solution is obtained by solving numerically equation (4.1) and applying the constraints defined above. Our solution satisfies the compatibility condition  $f_2 = f_3$ , so that this shows that both detached segments can be connected through a segment in full contact with the wall. There is no solution of this kind for  $\epsilon_4 < R/S < \epsilon_3$ , where  $\epsilon_4 = 0.323$ . This can be explained by the fact that the solution for  $\epsilon_3 < \epsilon$  cannot be continuously connected with the solution for  $\epsilon < \epsilon_4$ . Force  $Q_4$  is perpendicular to the segment between points 0 and 1 in figure 8b, but the equivalent force has a radial direction in figure 6d. Hence, somehow the force  $Q_4$  must rotate between the values  $\epsilon_3$  and  $\epsilon_4$ . To explain this rotation, we need to include the thickness of the sheet in the analysis, so that our approach is no longer valid in this case.

Figure 8d shows the sheet shape for  $R/S = \epsilon_5 = 0.263$ . At this condition, a new contact is made between both detached segments. This contact adds a pair of point forces, so that there are now seven point forces, as figure 9b shows. We can use similar numerical analysis to obtain the shape of the sheet, although the technical difficulties increase. It is necessary to solve the equations for five different segments to obtain the unknown parameters. This solution is valid until

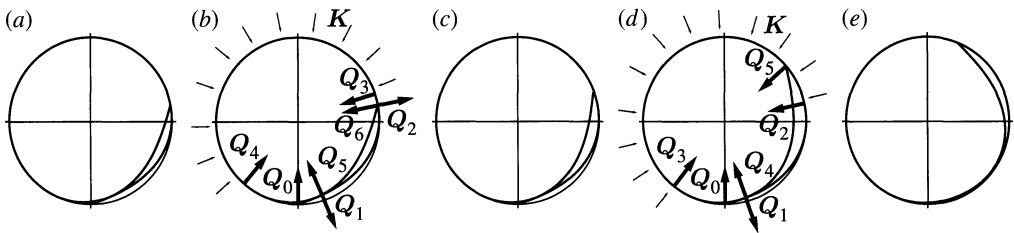


Figure 9. Sketch of the coiled sheet for (a)  $R/S = \epsilon_5$ , (b)  $R/S = 0.255$ , (c)  $R/S = \epsilon_6$ , (d)  $R/S = 0.240$  and (e)  $R/S = \epsilon_7$ .

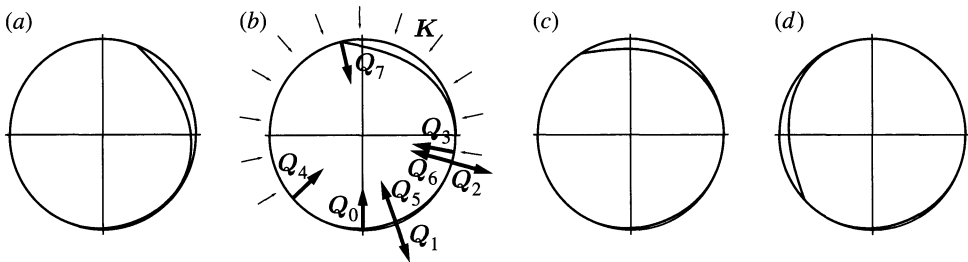


Figure 10. Sketch of the coiled sheet for (a)  $R/S = \epsilon_7$ , (b)  $R/S = 0.210$ , (c)  $R/S = \epsilon_8$  and (d)  $R/S = \epsilon_9$ .

point 6 meets point 3 and presses directly against the wall. At this configuration  $R/S = \epsilon_6 = 0.250$ , the length of the sheet is eight times the diameter. The corresponding sheet shape is shown in figure 9c.

For  $\epsilon < \epsilon_6$ , the end of the inner detached segment rests over the part of the coil in contact with the tube wall. There are now six point forces over the sheet and a total of four segments. Further decreases of the radius make point 5 move along the wall and the curvature in point 4 decrease. The behaviour of the sheet at point 4 is very similar to the one observed for point 1 in figure 5. At the value  $R/S = \epsilon_7 = 0.224$ , the curvature at point 4 matches the curvature of point 1, so that a region of contact starts to develop for  $\epsilon < \epsilon_7$ .

Figure 10b shows the forces for  $\epsilon < \epsilon_7$ . The region of contact between the inner and outer detached segments spans the arc length from point 1 to point 2 (or from point 5 to point 6). It is noteworthy that the Euler equation is still valid in this region. This is explained by using the equations in (2.1). The balance of forces for each segment along the contact region is

$$\text{and } \left. \begin{aligned} \partial_s \mathbf{F}^i + \mathbf{K} &= \mathbf{0} \\ \partial_s \mathbf{F}^e - \mathbf{K} &= \mathbf{0}, \end{aligned} \right\} \quad (4.2)$$

where  $\mathbf{F}^i$  and  $\mathbf{F}^e$  are the cross-sectional forces for the inner and outer segment in contact, respectively. The external force is only due to the interaction between both segments; therefore, the total cross-sectional force  $\mathbf{F} = \mathbf{F}^i + \mathbf{F}^e$  for the joined sheet follows the equation  $\mathbf{F} = F_1 \mathbf{e}_1 + F_2 \mathbf{e}_2 = \text{cte}$ . Moreover, the torque balance for each segment in the contact region is

$$\text{and } \left. \begin{aligned} \partial_s \mathbf{M}^i + \mathbf{t}^i \times \mathbf{F}^i &= \mathbf{0} \\ \partial_s \mathbf{M}^e + \mathbf{t}^e \times \mathbf{F}^e &= \mathbf{0}. \end{aligned} \right\} \quad (4.3)$$

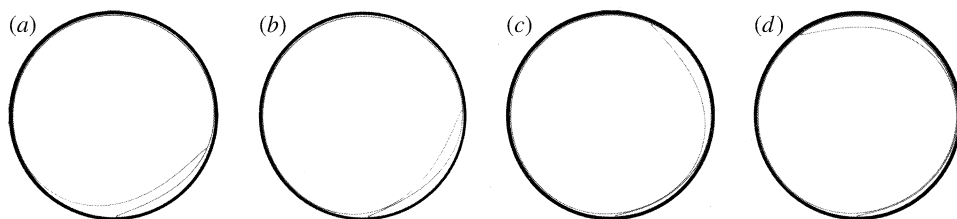


Figure 11. Photographs for a coil made of mica for different values of the parameter  $R/S$ . (a)  $R/S=0.28$ , (b)  $R/S=0.26 \approx \epsilon_5$ , (c)  $R/S=0.22 \approx \epsilon_7$  and (d)  $R/S=0.20 \approx \epsilon_8$ .

Both segments have the same tangent, hence  $\mathbf{t} = \mathbf{t}^i = \mathbf{t}^e$  and  $\mathbf{M}^i = \mathbf{M}^e$ . Adding equations (4.3) and using the Bernoulli–Euler theory, we conclude that the tangent angle satisfies the equation

$$2B\ddot{\phi} - F_2 \sin \phi - F_1 \cos \phi = 0, \quad (4.4)$$

along the contact region. This is the Euler equation for a sheet with twice the rigidity of the original one. Thus, we need to solve again the same system of equations in (4.1) for each segment of the sheet. A numerical solution shows how the contact region expands as the radius is reduced. At  $R/S = \epsilon_8 = 0.203$ , point 6 meets point 3, thence point 6 is in direct contact with the tube wall and must have the curvature  $1/R$ . The inner detached segment satisfies, at points 6 and 7, the same boundary conditions that we used to obtain the universal shape in §2. The take-off point at point 6 is in an angle  $\approx 86.8^\circ$  from the vertical line, so that a clockwise rotation of figure 10c in the same amount reproduces figure 1.

As the radius is further decreased, the inner detached segment moves along the tube, while the structure for the outer detached region remains intact. Both segments do not interact until point 7 in figure 10b meets point 4. This happens for  $R/S = \epsilon_9 = 0.172$  figure 10d. It is interesting to observe that the part of the tube wall not in contact with the sheet spans an angle of  $\beta_e \approx 134^\circ$ . This is more than one-third of the total perimeter and larger than the opening angle  $\beta$ . The angle  $\beta_e$  diminishes as the number of layers increases, as we will study in §5.

We have experimentally checked the configurations predicted by our numerical solutions. Figure 11 shows different shapes for a mica sheet as the radius of the tube decreases. Friction was minimized by shaking the tube before each photograph was taken. The observed shapes are consistent with figures 4–10. Additionally, the transitions can be followed by using the average pressure as the order parameter. Figure 12 shows the value of the pressure for  $\epsilon_9 < R/S < 1$ . It is an irregular function of the radius size. The fluctuations are obviously related to the different events observed in the coiling process.

## 5. A sheet with $N$ layers

For  $R/S < \epsilon_9$ , the inner detached segment starts to press the part of the coil that is not in contact with the tube wall. This makes the angle  $\beta_e$  smaller. At some critical radius, a point along the inner segment touches the coil in a similar way to that shown in figure 8d. The curvature of the innermost layer at this new contact point is larger than the curvature of the underlying layer. However, this curvature decreases as the radius is further decreased. At a critical value of the radius, both curvatures match, and a region of contact is produced. This region of contact now has three

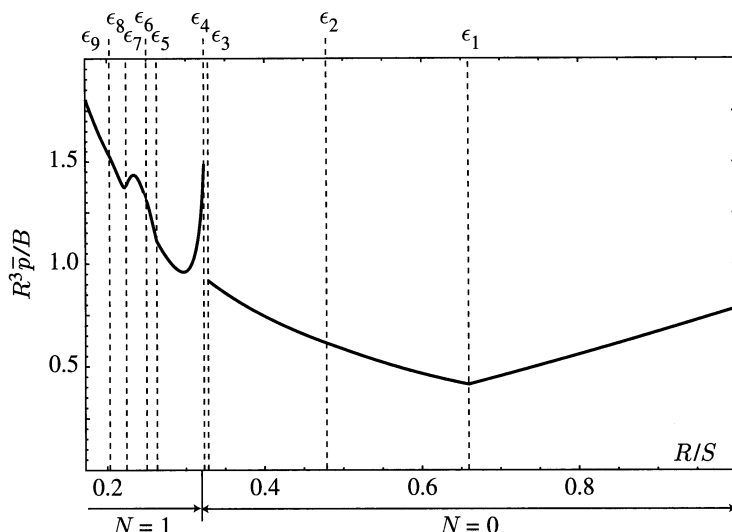


Figure 12. The dimensionless average pressure  $R^3 \bar{p}/B$  as a function of the radius size for  $\epsilon_9 < R/S < 1$ . The discontinuity for  $\epsilon_4 < R/S < \epsilon_3$  is explained in the text.

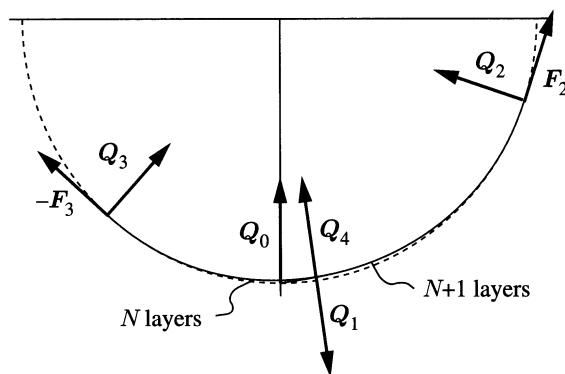


Figure 13. The outer detached region for  $N=3$ .

layers. Finally, this region expands and one of its boundaries reaches the curvature of the tube wall. At this condition, the detached region in the innermost layer restores the universal shape that we reported in §2. The sheet shape looks similar to figure 10*d*, although the coil now has  $N=2$ .

We can study the configuration observed in figure 10*d* for  $N$  layers. Figure 13 shows the part of the coil not in contact with the tube wall. The segment between points 0 and 1 has one layer and prevents the coil making contact with the tube wall. It joins the coil at point 1, so that the coil has  $N+1$  layers between points 1 and 2. At point 2, the  $N+1$  layers make contact with the tube wall, so that their curvature is  $1/R$ . At some distance from point 2, emerges the inner detached segment (not shown in figure 13) with the universal shape described in §2. This implies that the coil has  $N$  layers at point 3.

Five point forces are needed to understand the detachment of the coil from the wall. They are

$$\mathbf{Q}_0 = -q_0 \mathbf{e}_1, \quad \mathbf{Q}_1 = q_1 \mathbf{n}(\phi_1), \quad \mathbf{Q}_2 = -q_2 \mathbf{n}(\phi_2), \quad \mathbf{Q}_3 = -q_3 \mathbf{n}(\phi_3) \quad \text{and} \quad \mathbf{Q}_4 = -\mathbf{Q}_1.$$

The rest of the coil applies a cross-sectional force  $\mathbf{F}_3 = N(B/R^2)\mathbf{t}(\phi_3)$  at point 3 and  $\mathbf{F}_2 = (N+1)(B/R^2)\mathbf{t}(\phi_2)$  at point 2 (figure 13). Here, we use the results obtained in §2b: each layer with curvature  $1/R$  has the same cross-sectional force  $f=B/R^2$  provided by the inner detached segment. Force balance dictates the equilibrium condition,

$$\mathbf{F}_2 - \mathbf{F}_3 + \mathbf{Q}_2 + \mathbf{Q}_3 + \mathbf{Q}_0 = 0. \quad (5.1)$$

Equation (2.8) connects point 0 with point 2 and gives the magnitude of force  $\mathbf{Q}_0$  as  $\tilde{q}_0 = 1/2 \sin \phi_0$ . Here,  $\tilde{q}_0 = R^2 q_0/B$  is the dimensionless form of force  $q_0$ . This identity and equation (5.1) give the magnitudes of forces  $\mathbf{Q}_2$  and  $\mathbf{Q}_3$  as a function of the angles  $\{\phi_0, \phi_2, \phi_3\}$ . We obtain

$$\tilde{q}_2 = \frac{1}{\sin(\phi_3 - \phi_2)} [(N+1)\cos(\phi_3 - \phi_2) - N - \sin \phi_3/2 \sin \phi_0]$$

and

$$\tilde{q}_3 = \frac{1}{\sin(\phi_3 - \phi_2)} [N \cos(\phi_3 - \phi_2) - (N+1) + \sin \phi_3/2 \sin \phi_0],$$

where  $\tilde{q}_2$  and  $\tilde{q}_3$  are the dimensionless form of forces  $q_2$  and  $q_3$ , respectively. Using equation (2.1), we can obtain the cross-sectional force along the segment between points 0 and 1 as  $\mathbf{F} = -\mathbf{Q}_0$ . Similar analysis shows that the cross-sectional forces along the segment defined by points 1 and 2, and 3 and 4 are  $\mathbf{F} = \mathbf{F}_2 + \mathbf{Q}_2$  and  $\mathbf{F}_3 - \mathbf{Q}_3$ , respectively. These relations allow us to obtain the Euler equation for each segment. The Euler equation for the segment between points 0 and 1 is  $R^2 \ddot{\phi} - \tilde{q}_0 \cos \phi = 0$ . A first integration gives the curvature as  $R\dot{\phi} = (2\tilde{q}_0)^{1/2} (\sin \phi - \sin \phi_0)^{1/2}$ , where we have used the condition that the curvature is zero at point 0. We can obtain the shape of the sheet by using equation (4.1). The coordinates of the segment between points 0 and 1 are given by

$$\left. \begin{aligned} x_{01}/R &= - \int_{\phi_0}^{\phi} d\phi \frac{\sin \phi}{(2\tilde{q}_0)^{1/2} (\sin \phi - \sin \phi_0)^{1/2}} + 1 \\ \text{and} \\ y_{01}/R &= \int_{\phi_0}^{\phi} d\phi \frac{\cos \phi}{(2\tilde{q}_0)^{1/2} (\sin \phi - \sin \phi_0)^{1/2}}, \end{aligned} \right\} \quad (5.2)$$

where we have used the boundary conditions  $(x(\phi_0), y(\phi_0)) = (R, 0)$ . The Euler equation for the next segment is  $(N+1)R^2 \ddot{\phi} + \tilde{q}_2 \cos(\phi - \phi_2) + (N+1) \sin(\phi - \phi_2) = 0$ . A first integration with the boundary condition  $\dot{\phi}(\phi_2) = 1/R$  gives, for the curvature,  $R\dot{\phi} = [2 \cos(\phi - \phi_2) - 1 - 2\tilde{q}_2 \sin(\phi - \phi_2)/(N+1)]^{1/2}$ . Using point 2 as the starting point, we obtain the coordinates of this segment as

$$\left. \begin{aligned} x_{12}/R &= \int_{\phi}^{\phi_2} d\phi \frac{\sin \phi}{[2 \cos(\phi - \phi_2) - 1 - 2\tilde{q}_2 \sin(\phi - \phi_2)/(N+1)]^{1/2}} + \cos \phi_2 \\ \text{and} \\ y_{12}/R &= - \int_{\phi}^{\phi_2} d\phi \frac{\cos \phi}{[2 \cos(\phi - \phi_2) - 1 - 2\tilde{q}_2 \sin(\phi - \phi_2)/(N+1)]^{1/2}} + \sin \phi_2. \end{aligned} \right\} \quad (5.3)$$

Finally, we study the segment between points 3 and 4. The Euler equation is  $NR^2 \ddot{\phi} - \tilde{q}_3 \cos(\phi - \phi_3) + N \sin(\phi - \phi_3) = 0$  and the curvature is  $R\dot{\phi} = [2 \cos(\phi - \phi_3)$

$-1 + 2\tilde{q}_3 \sin(\phi - \phi_3)/N]^{1/2}$ , where we have used the condition  $\dot{\phi}(\phi_3) = 1/R$ . The coordinates starting from point 3 are

$$\left. \begin{aligned} x_{34}/R &= - \int_{\phi_3}^{\phi} d\phi \frac{\sin \phi}{[2 \cos(\phi - \phi_3) - 1 - 2\tilde{q}_3 \sin(\phi - \phi_3)/N]^{1/2}} + \cos \phi_3 \\ \text{and} \\ y_{34}/R &= - \int_{\phi_3}^{\phi} d\phi \frac{\cos \phi}{[2 \cos(\phi - \phi_3) - 1 - 2\tilde{q}_3 \sin(\phi - \phi_3)/N]^{1/2}} + \sin \phi_3. \end{aligned} \right\} \quad (5.4)$$

The coordinates along these three segments must coincide at point 1, so that we have the identities

$$x_{01}(\phi_1) = x_{12}(\phi_1) = x_{34}(\phi_1 + 2\pi) \quad \text{and} \quad y_{01}(\phi_1) = y_{12}(\phi_1) = y_{34}(\phi_1 + 2\pi).$$

These four relations completely define the values of the four unknown parameters  $\{\phi_0, \phi_1, \phi_2, \phi_3\}$ . These equations can be solved numerically to obtain the parameters and the subtended angle  $\beta_e = (2\pi - \phi_3) + \phi_2$ . We find that this angle follows the scaling  $\beta_e \sim N^{-1/3}$ . We also obtain  $\beta_e \sim \phi_2 \sim 2\pi - \phi_3 \sim N^{-1/3}$  and  $\phi_1 \sim \phi_0 \sim N^{-2/3}$ . A more precise analysis can be made by using these results to expand equations (5.2)–(5.4) at point 1. We write  $N = \eta N$ ,  $\beta_e = \eta^{1/3} \beta_e$ ,  $\phi_0 = \eta^{2/3} \phi_0$ , etc., where  $\eta$  is an expansion parameter. In powers of  $\eta$ , it yields, for the first two orders,

$$\left. \begin{aligned} x_{01}(\phi_1)/R &= 1 - \frac{2}{3}(\phi_1 + 2\phi_0)(\phi_1 - \phi_0)^{1/2} \eta^{4/3} \\ \text{and} \\ y_{01}(\phi_1)/R &= 2[\phi_0(\phi_1 - \phi_0)]^{1/2} \eta^{2/3} - \frac{1}{6}[\phi_0(\phi_1 - \phi_0)]^{1/2} (2\phi_0^2 + \phi_0\phi_1 + \phi_1^2) \eta^2, \end{aligned} \right\} \quad (5.5)$$

$$\left. \begin{aligned} x_{12}(\phi_1)/R &= 1 + \frac{2\phi_2^3\phi_3' - N\phi_0(\phi_2 + \phi_3')(12\phi_1^2 + 2\phi_2^3\phi_3' + \phi_2^4)}{24N\phi_0(\phi_2 + \phi_3')} \eta^{4/3} \\ \text{and} \\ y_{12}(\phi_1)/R &= \phi_1 \eta^{2/3} + \frac{-3\phi_2^2\phi_3' + N\phi_0\phi_2^2(\phi_2^2 + 4\phi_2\phi_3' + 3\phi_3'^2)}{12N\phi_0(\phi_2 + \phi_3')} \eta^1, \end{aligned} \right\} \quad (5.6)$$

$$\left. \begin{aligned} x_{34}(\phi_1 + 2\pi)/R &= 1 + \frac{2\phi_3'^3\phi_2 - N\phi_0(\phi_3' + \phi_2)(12\phi_1^2 + 2\phi_3'^3\phi_2 + \phi_3'^4)}{24N\phi_0(\phi_3' + \phi_2)} \eta^{4/3} \\ \text{and} \\ y_{34}(\phi_1 + 2\pi)/R &= \phi_1 \eta^{2/3} + \frac{-3\phi_3'^2\phi_2 + N\phi_0\phi_3'^2(\phi_3'^2 + 4\phi_3'\phi_2 + 3\phi_2^2)}{12N\phi_0(\phi_3' + \phi_2)} \eta^1. \end{aligned} \right\} \quad (5.7)$$

Here,  $\phi_3' = 2\pi - \phi_3$  is the angle of point 3 taken from the vertical direction. Comparing equations (5.6) and (5.7), we conclude that  $\phi_2 = \phi_3'$ , so that both sets of equations are now equivalent. The  $y$  coordinates in equations (5.5) and (5.6) are equal at the first order if  $\phi_1 = 2\phi_0$ . We now observe that there is not a term of the order of  $\eta$  in equations (5.5) for the  $y$  coordinate, so that this term must be zero in equations (5.6). It yields the condition  $8N\phi_0\phi_2 - 3 = 0$ . Finally, we compare the

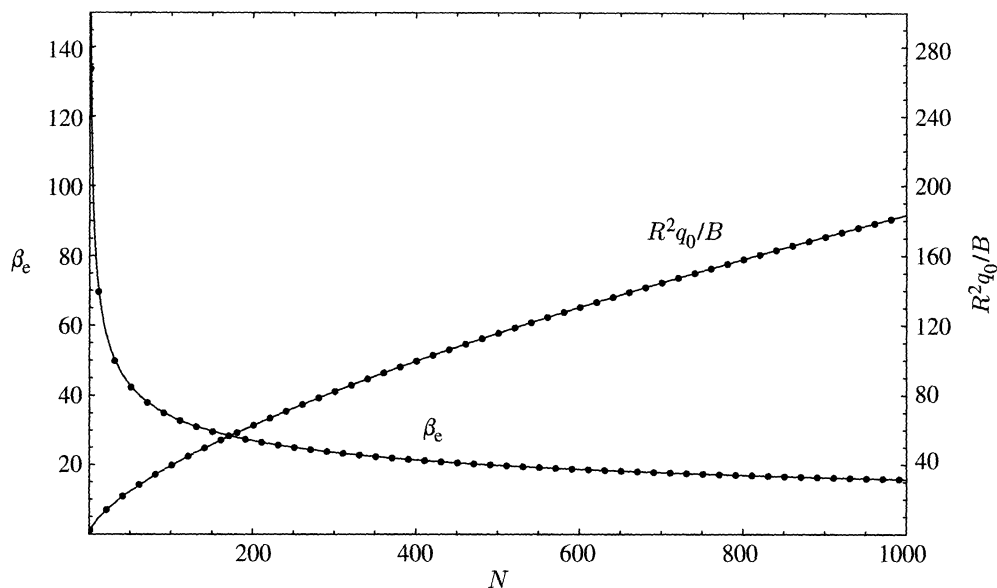


Figure 14. Dotted lines show the numerical results for  $\beta_e$  (in deg.) and the dimensionless force  $R^2 q_0/B$ . The solid lines give the asymptotic approximations  $(2\sqrt{3})/(2^{1/3})N^{-1/3}$  and  $(22^{2/3})/(\sqrt{3})N^{2/3}$  for the angle  $\beta_e$  and the force, respectively.

second order for the  $x$  coordinate of equations (5.5) with the equivalent expression in equations (5.6). They must be equal. This gives the condition  $16N\phi_0^3 + \phi_2^3 - 3N\phi_0\phi_2^4 = 0$ . We solve the last two relations to find  $\phi_2 = \phi_3' = \beta_e/2 = (\sqrt{3}/2^{1/3})N^{-1/3}$  and  $\phi_0 = \phi_1/2 = ((\sqrt{3})/(42^{2/3}))N^{-2/3}$ . Figure 14 shows a comparison of our analytical results with the numerics. It can be observed that our asymptotic analysis works, even for a small number of layers. In fact, we obtain, for  $N=1$ , an angle  $\beta_e \approx 158^\circ$  that is  $25^\circ$  off the exact value obtained in §4.

The origin of the scaling for  $\beta_e$  can be partially understood by considering the force equilibrium of the coil. Force  $Q_0$  must balance the pressure applied by the tube wall along the sheet between points 2 and 3. This pressure  $p$  is of the order of  $\sim NB/R^3$ , as we found in §2*b*. Since the pressure applied in the upper part of the coil is not balanced in a sector of length  $\sim R\beta_e$  in the lower part of the coil, it gives a net downward force  $\sim \beta_e NB/R^2$ . Force balance yields  $q_0 \sim \beta_e NB/R^2$ . Using the identity  $R^2 q_0/B = 1/2 \sin \phi_0 \sim 1/\phi_0$ , we obtain the condition  $1 \sim N\phi_0\beta_e$ . This relation is satisfied by the scaling we found above.

Our scaling relations show that the point forces at the contact with the wall  $q_0$ ,  $q_2$  and  $q_3$  increase as  $\sim N^{2/3}$ . In this limit, the contribution to the average pressure  $\bar{p}$  of these point forces is negligible compared with the pressure made by the coil between points 2 and 3. In addition, when the number of layers increases, the region of contact expands to almost the full perimeter. Thus, for sufficient number of layers, the main contribution to the average mechanical pressure comes from the local pressure defined in (2.7), and then both quantities must coincide.

It is clear that our analysis for the outer detached region will be valid until the thickness plays a role in the configuration depicted in figure 13. Point 0 can interact with the layer above if the thickness is of the order of the distance between them.

An estimation of this distance is given by the condition  $R - x_{01}(\phi_1) \sim t$  or, by using (5.5),  $(1/(42^{1/3}N^{4/3})) \sim t/R$ . Thus, the number of layers must be smaller than  $(1/22^{3/4})(R/t)^{3/4}$ . For the largest value of  $R/t$  in figure 3, this gives  $N \approx 50$ . This number should be sufficient to observe the proposed scaling.

## 6. Conclusions

We have studied the simplest configuration to confine an elastic sheet inside a cylinder. To minimize the bending energy, the sheet decreases its curvature by staying close to the wall. This makes a spiral of pitch  $t$  and increasing curvature in proportion to the number of times the sheet is coiled. Our results show how the extremities of the spiral, which have to be straight and detached from the coil since there are not applied moments at the ends, provide the necessary torques to bend the sheet. To study the shape of the sheet at its extremities, we assume that thickness is negligible, although it is possible to see how our results will change when thickness is included in the analysis. The effective radius  $R_{\text{eff}}$  of the inner part of the coil is roughly  $R_{\text{eff}} \approx R - tN = R(1 - p/2)$ , where  $p$  is the packing ratio  $p = 2St/\pi R^2$  (Donato *et al.* 2003). Thus, all our results in §2a for the inner detached segment can be corrected replacing  $R$  by this effective radius. Accordingly, this will change the size of the inner detached segment, but not its shape. Therefore, the angles defined for the inner detached segment will not change with the packing ratio. Our analysis for the coil and outer detached segment, however, are valid only when  $N \ll (1/22^{3/4})(R/t)^{3/4}$  or  $pN^{1/3} \ll 1$ .

The simplicity of our arguments suggests that a detached region can be found in other geometries. A fibre forced to coil inside a tube will be unstable if it is allowed to deform out of plane. In that case, bending energy is minimized by a helical shape, so that the whole fibre is in contact with the wall except for two segments at the extremities. Once again, these detached segments are required to obtain the torques that bend the fibre into a helical shape. Our analysis can also be applied to three-dimensional deformations of sheets. The Euler equation accounts not only for arbitrary planar deformations of rods, but also conical deformations of surfaces (Cerdeña & Mahadevan 2005; Boué *et al.* 2006). It is straightforward to see that a complete analogy can be formulated between the results of this paper, which focuses on planar deformations, and similar phenomena that are observed for conical shapes. For instance, a sheet can be coiled into a conical shape, as anyone who has ever rolled a paper to make a blowgun dart knows. In addition, looking along the cone axis, the inner end of the sheet detaches from the coil and again shows the configuration observed in figure 1.

We thank Juliano Denardin for providing the metal strip used in the experiments, and Sidney Nagel and Aaron Dinner for useful comments. We also thank the Chicago–Chile Materials Collaboration supported by the National Science Foundation under Award DMR-0303072. E.C. and V.R. acknowledge the support of Anillo N° ACT 15, FONDAF grant no. 11980002 and FONDECYT grant no. 1050083.

## References

Boué, L. & Katzav, E. 2007 Folding of flexible rods confined in 2D space. *Europhys. Lett.* **80**, 54 002. (doi:10.1209/0295-5075/80/54002)

*Proc. R. Soc. A* (2008)

- Boué, L., Adda-Bedia, M., Boudaou, A., Cassani, D., Couder, Y., Eddi, A. & Trejo, M. 2006 Spiral patterns in the packing of flexible structures. *Phys. Rev. Lett.* **97**, 166 104. (doi:10.1103/PhysRevLett.97.166104)
- Cerda, E. & Mahadevan, L. 2005 Confined developable elastic surfaces: tubes, cones and the elastica. *Proc. R. Soc. A* **461**, 671. (doi:10.1098/rspa.2004.1371)
- Cerda, E., Chaieb, S., Melo, F. & Mahadevan, L. 1999 Conical dislocations in crumpling. *Nature* **401**, 46–50. (doi:10.1038/43395)
- Cohen, A. & Mahadevan, L. 2003 Kinks, rings, and rackets in filamentous structures. *Proc. Natl Acad. Sci. USA* **100**, 12 141. (doi:10.1073/pnas.1534600100)
- Donato, C. C., Gomes, M. A. F. & de Souza, R. E. 2002 Crumpled wires in two dimensions. *Phys. Rev. E* **66**, 015 102. (doi:10.1103/PhysRevE.66.015102)
- Donato, C. C., Gomes, M. A. F. & de Souza, R. E. 2003 Scaling properties in the packing of crumpled wires. *Phys. Rev. E* **67**, 026 110. (doi:10.1103/PhysRevE.67.026110)
- Landau, L. D. & Lifshitz, E. M. 1997 *Theory of elasticity*, 3rd English edn. Oxford, UK: Butterworth-Heinemann Publishing.
- Love, A. E. H. 1944 *A treatise on the mathematical theory of elasticity*. New York, NY: Dover.
- Mahadevan, L. & Keller, J. B. 1999 Periodical folding of elastic sheets. *SIAM Rev.* **41**, 115. (doi:10.1137/S0036144598339166)
- Roman, B. & Pocheau, A. 1999 Buckling cascade of thin plates: forms, constraints and similarity. *Europhys. Lett.* **46**, 602. (doi:10.1209/epl/i1999-00306-3)
- Struik, D. J. 1988 *Lectures on classical differential geometry*. New York, NY: Dover.
- Witten, T. 2007 Stress focusing in elastic sheets. *Rev. Mod. Phys.* **79**, 643. (doi:10.1103/RevModPhys.79.643)
- Witten, T. A. & Li, H. 1993 Asymptotic shape of a fullerene ball. *Europhys. Lett.* **23**, 51–55. (doi:10.1209/0295-5075/23/1/009)